Bioprinted integrated gradient biomechanical signal-tailored osteosarcoma model: advancing insights into tumor development and drug screening

Xuelian Mi[1#]. Ya Ren[2#]. Hanbo Wang[3#]. Lei Qiang[4]. Weiqing Kong[5]. Hui Wang[6]. Xue Yang[2]. Yihao Liu[7]. Han Yang[7]. Di Xiao[8]. Zhenjiang Ma[7]. Guoxing Xu[9]. Changru Zhang[7]*. Jinwu Wang[1,7]*

[1]Institute of Biomedical Engineering, College of Medicine, Southwest Jiaotong University, Chengdu 610031, Sichuan, China

[2]State Key Laboratory of Biotherapy and Cancer Center, West China Hospital, Sichuan University, 610041 Chengdu, China; Southwest Jiaotong University College of Medicine, Chengdu, 610031, China

[3]Orthopaedic Bioengineering Research Group, Division of Surgery and Interventional Science, University College London, London, HA7 4LP, United Kingdom

[4]Key Laboratory of Advanced Technologies of Materials (MOE), School of Materials Science and Engineering, College of Medicine, Southwest Jiaotong University, Chengdu, 610031, PR China

[5]Department of Spinal Surgery, The Affiliated Hospital of Qingdao University, No. 59 Haier Road, Qingdao, Shandong Province, 266000 China

[6]Engineering Research Center of Intelligent Rehabilitation of Traditional Chinese Medicine，Ministry of Education；School of Rehabilitation Science, Shanghai University of Traditional Chinese Medicine, Shanghai 201203, China

[7]Shanghai Key Laboratory of Orthopedic Implant, Department of Orthopedics, Ninth People's Hospital Affiliated to Shanghai Jiao Tong University School of Medicine, Shanghai 200011, China; School of Biomedical Engineering, Shanghai Jiao Tong University, Shanghai, 200030, China

[8]Liuzhou Traditional Chinese Medical Hospital, Guangxi University of Chinese Medicine, 545001, Liuzhou, Guangxi, China

[9]Department of Orthopaedics, Jiading District Anting Hospital of Shanghai, Shanghai 201805, China

Xuelian Mi, Ya Ren, and Hanbo Wang contributed equally to this work.

* Corresponding authors
Changru Zhang：zcr_ecust@163.com
Jinwu Wang：wangjw-team@shsmu.edu.cn

Abstract

In current osteosarcoma research and drug screening, in vitro 3D models are favored for overcoming the limitations of traditional models. In in vitro 3D models, tumor microenvironment simulation, especially mechanical microenvironment, is crucial for tumor biological effects. However, current in vitro tumor model construction for osteosarcoma is often limited to a single mechanical signal, which fails to simulate the diversity of osteosarcoma mechanical stimuli. In this study, we utilized embedded bioprinting technology and multiple response properties of calcium ions in soft stiffness systems, hard stiffness systems, and osteosarcoma cell biological functions to construct an integrated gradient biomechanical signal-tailored osteosarcoma model. Specifically, we achieved this by printing a fibrinogen bioink containing calcium ions and osteosarcoma tumor spheroids within an extracellular matrix composed of methacryloylated alginate, methacryloylated gelatin, and thrombin, which is rich in polysaccharides and proteins and exhibits self-healing properties. In vitro and in vivo studies showed that the integrated gradient biomechanical signal-tailored osteosarcoma model enhanced tumor stemness, proliferation and migration, successfully reproduced the nest-like structure of cancer, and provided an in vitro research platform closer to a natural tumor. In conclusion, this study proposes a novel integrated gradient biomechanical signal-tailored osteosarcoma model construction system that provides a new strategy for the clinical understanding of tumor development, drug screening, and exploration of drug resistance and metastasis mechanisms.

Keywords

3D bioprinting. Gradient biomechanical signal-tailor. Osteosarcoma model. Tumor development. Drug screening

Introduction

Osteosarcoma is the most common malignant bone tumor, characterized by high aggressiveness and heterogeneity, and poses great challenges for patient survival and treatment[1, 2]. In vitro tumor models have become important tools for the study of malignant tumors because of their advantages, such as high-throughput drug screening, no animal ethical issues, cost-effectiveness, and applications in mechanistic studies and personalized medicine. Over the past few decades, developments such as simple two-dimensional monolayer tumor cell cultures and xenograft animal tumor models have provided important insights into osteosarcoma research and the development of new therapies. Two-dimensional monolayer tumor cell culture models lose tumor-specific morphology, function, and metabolic activity and lack cell–cell and cell–extracellular matrix (ECM) interactions. In addition, the biology of tumor cells is altered in two-dimensional culture systems, leading to research artifacts and a high failure rate for drug treatment regimens. Meanwhile, the applications of animal tumor models face limitations such as long modeling time, high cost, and animal ethics[3, 4].

In recent years, in vitro 3D tumor models have received widespread attention because of their likeness to the 3D structure of in vivo tumor tissues and more effective simulation of the tumor microenvironment. The construction of the tumor mechanical

microenvironment in in vitro tumor models, particularly ECM stiffness in the tumor mechanical microenvironment, affects tumor proliferation, angiogenesis, metabolism, invasion, migration, and metastasis[5, 6]. During tumor development, tumor cells remodel the surrounding ECM, and the ECM around the tumor forms a gradient structure with a soft inner layer and a hard outer layer[7, 8]. Although the ECM mechanical characterization for osteosarcoma is more limited at present, we can gain some insights from the studies of other types of tumors. Xu et al.[9] found that the Young's modulus of ovarian cancer cells is about 0.8 kPa as measured by atomic force microscopy (AFM). Similarly, a study by Plodinec et al. [10] revealed that the Young's modulus of breast cancer cells is approximately 0.75 kPa. Simultaneously, mechanical signals from the ECM regulate the biological functions of tumor cells. Macroscopically, osteosarcoma typically occurs in the proximal metaphysis of long bones[11], which is a region containing more collagenous bone tissue. With the growth of osteosarcoma, osteosarcoma tissues directly contact the surrounding collagenous bone tissues to form a macroscopically hard biomechanical microenvironment, which gradually undergoes protein secretion and deposition during development, forming a microcosmically soft biomechanical microenvironment inside the solid tumor[12]. Therefore, it is of great significance to construct an in vitro tumor model with tailored gradient biomechanical signals to simulate the gradient biomechanical signal characteristics of natural solid tumors and to reproduce the biological phenotype of natural tumor tissues to study the mechanisms of tumorigenesis, drug screening, treatment, drug resistance, and metastasis. Currently, numerous researchers have constructed in vitro three-dimensional models of osteosarcoma to carry out a series of studies; however, they have not reproduced in vitro osteosarcoma models constructed with gradient biomechanical signals to mimic the gradient biomechanical signal characteristics of natural solid tumors[13, 14, 15, 16].

Gelatin, derived from type I collagen, is a core component of the ECM in tumor and bone microenvironments. Upon reaction with methacrylic anhydride, gelatin can be converted into photocrosslinkable gelatin methacrylate (GelMA), widely used to mimic the natural ECM in in vitro disease models[17, 18]. Alginate, a polysaccharide extracted from natural seaweeds, possesses excellent biocompatibility but relatively weak mechanical properties. However, when reacted with methacrylic anhydride, alginate is transformed into methacrylated alginate (AlgMA), which retains its excellent biocompatibility and superior mechanical properties. When GelMA and AlgMA undergo crosslinking under UV irradiation, they form hydrophilic biopolymer hydrogels with three-dimensional network structures. Additionally, calcium ions form physical crosslinks with the carboxyl groups in AlgMA via electrostatic interactions, resulting in the formation of egg-box structures and significantly enhancing the structural integrity of the hydrogels[19, 20, 21]. In recent years, enzymatically crosslinked fibrin hydrogels based on fibrinogen, thrombin (Th), or transglutaminase (TG) have gained widespread attention owing to their ability to form stable three-dimensional structures, providing suitable microenvironments for in vitro tumor models[22, 23]. Notably, calcium ions play a pivotal role in our unique model system, demonstrating distinctive effects not only within soft stiffness systems and hard

stiffness systems, but also exhibiting multifaceted response characteristics in regulating the biological functions of osteosarcoma cells. First, through integration with AlgMA, calcium ions form a reversible network structure via physical crosslinking, greatly enhancing the system stability. Second, calcium ions activate transglutaminase, promoting the covalent crosslinking of fibrin peptides formed after thrombin cleavage, thereby forming stable fibrin hydrogels. Additionally, calcium ions participate in and regulate key biological behaviors, such as the proliferation, migration, and invasion of osteosarcoma cells.

Currently, bioprinting technology, an emerging 3D tissue engineering method, is a powerful tool for constructing simulation models. By precisely controlling the arrangement of biomaterials and the distribution of cells, bioprinting technology can simulate the complex structure of in vivo tissues. Particularly in the field of tumor research, the application of bioprinting technology has provided groundbreaking opportunities, enabling the construction of more realistic and controllable tumor models[24, 25]. However, it is difficult to achieve high cell densities similar to those of natural tissues by co-mixing conventional bioinks with cells[26]. To address this challenge, we used pre-cultured tumor spheroids to achieve high cell density, pH, oxygen, nutrient and metabolic gradients, and necrotic region properties to mimic natural human solid tumors [27].

Therefore, we propose a fast and convenient design strategy for simulating the gradient biomechanical signal characteristics of osteosarcoma. A soft ECM adapted to the modulus of osteosarcoma cells was constructed to simulate a microscopic soft biomechanical microenvironment, and a hard biomechanical microenvironment adapted to the modulus of collagenous bone tissue was constructed to simulate a macroscopic hard biomechanical microenvironment. Specifically, we achieved this by printing a fibrinogen bioink containing calcium ions and osteosarcoma tumor spheroids within an extracellular matrix composed of methacryloylated alginate, methacryloylated gelatin, and thrombin, which is rich in polysaccharides and proteins and exhibits self-healing properties (Fig. 1). This innovative model not only simulates the gradient biomechanical signal characteristics of osteosarcoma but also provides us with an in vitro research platform that closely mimics natural tumors.

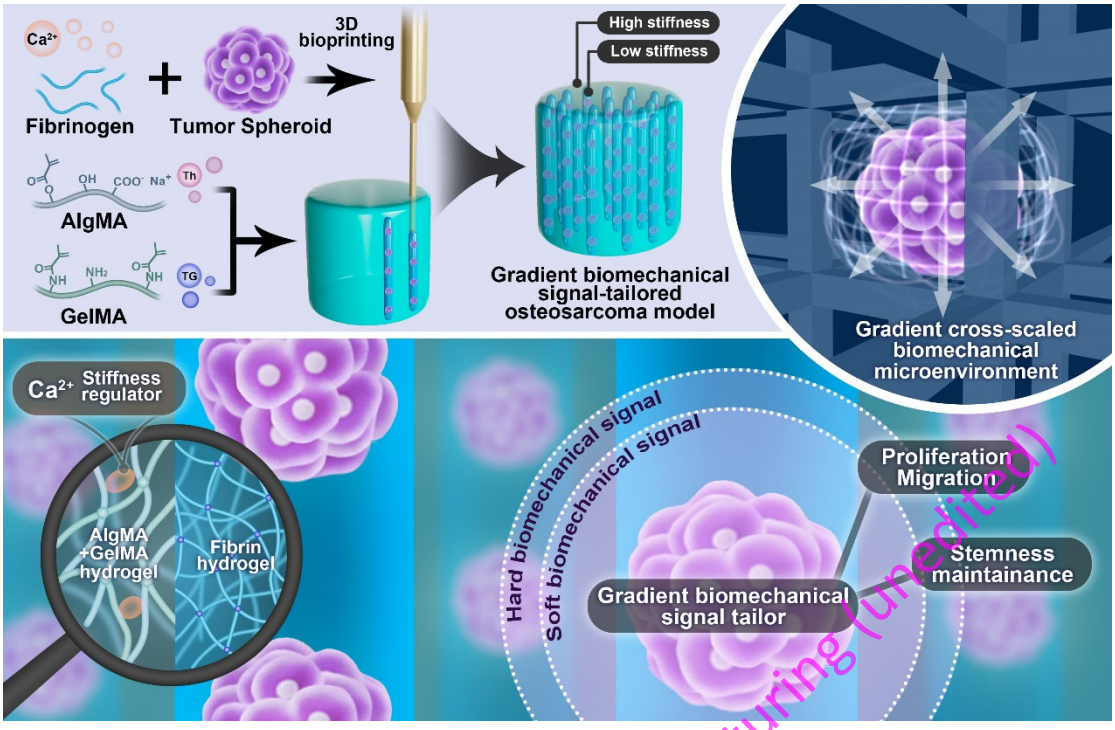

Fig.1 Schematic of the 3D bioprinting method for gradient biomechanical signal-tailored osteosarcoma models. Fibrinogen containing osteosarcoma tumor spheroids and calcium ions was used as a bioink for printing in an AlgMA/GelMA bioink bath supplemented with thrombin and transglutaminase. Thrombin and transglutaminase interacted with the fibrinogen and polymerized during the printing process, forming a soft fibrin hydrogel inside the hard AlgMA/GelMA hydrogel to construct an integrated gradient biomechanical signal-tailored osteosarcoma model (Ca^{2+}-G/OS).

Materials and methods

Materials and Reagents

Fibrinogen and thrombin were acquired from Yeasen Biotechnology (Shanghai, China). GelMA, AlgMA, phenyl-2,4,6-trimethylbenzoylphosphinate (LAP), and 96-well cell culture plates were obtained from EFL at Suzhou Intelligent Manufacturing Research Institute, China. Transglutaminase was acquired from Sigma-Aldrich. Lumbrokinase, doxorubicin, and methotrexate were acquired from Aladdin Reagent Co. (Shanghai, China). Rhodamine B and calcium chloride ($CaCl_2$) were acquired from Macklin (Shanghai, China). MG-63 (human osteosarcoma cell lines) was obtained from FuHeng Biology (Shanghai, China). Antibiotics (penicillin/streptomycin, PS) and Dulbecco's modified Eagle's medium (DMEM) were acquired from Gibco BRL (Shanghai, China). Fetal bovine serum (FBS) was acquired from Sigma-Aldrich.

Spheroid culture of osteosarcoma

The MG-63 cells were maintained in a temperature-controlled environment at 37°C and under 5% CO_2 atmosphere, following the manufacturer's guidelines. MG-63 cells were expanded until 80% confluence was reached and routinely passaged using trypsin. The cell culture medium was changed routinely every 2 days. Upon reaching

approximately 80% confluency, the cells were detached from the culture dishes using trypsin and subsequently suspended in cell culture media. According to the manufacturer's requirements, 3D tumor spheroids comprising MG-63 cells were fabricated using ultra-low adhesion 96U microplates (EFL, China). To achieve the ideal cellular density for producing dense 3D in vitro models, MG-63 cell suspensions with different cellular densities (10 000, 20 000, and 30 000 cells—SD-1, SD-2, and SD-3, respectively) were established. Cellular aggregation, size, and 3D spheroid morphological features were monitored over time via inverted fluorescence microscopy (Olympus CKX53, Japan). Tumor spheroids were observed every 12 h. These spheroids were cultured in a 37 °C and 5% CO_2 incubator.

Bioink preparation and bioprinting

GelMA (10% [w/v]) and LAP (0.5% [w/v]) were dissolved in deionized water at 55 ℃, and different concentrations of AlgMA were added to the solution. Solutions with final concentrations of 1%, 2%, 4%, and 10% of GelMA were prepared. The hydrogel solution was filtered by a 0.22 μm filter to remove bacteria. The hydrogel solution was carefully poured into a cylindrical mold and crosslinked under a UV lamp at a wavelength of 365 nm for 60s. After the cross-linking of covalent AlgMA/GelMA, the hydrogel was removed from the mold and soaked in a 1.8 mM $CaCl_2$ solution for 2 h to allow the ion cross-linking of AlgMA to occur.

The fibrinogen solution (10 mg/ml) was produced by dissolving lyophilized bovine plasma protein at 37 °C in sterile physiological saline with 1.8 mM $CaCl_2$ for 60 min. The solution was filtered through a 0.22 μm filter and stored at 4 °C. To prepare a stock solution of Th, lyophilized Th was reconstituted at 100 U/ml using physiological saline stored at −20 °C. Cross-linking was performed using physiological saline diluted to 10 U/ml Th and a 3% (w/v) TG working solution. The mixed solution of Th and TG was passed through a 0.22 μm filter and then stored at 4 °C under refrigeration.

The tumor model was fabricated using 3D bioprinting (Biobulid-S, China). Before printing, the 3D bio printer was sterilized with ultraviolet light on an ultra-clean table. Next, 500 pre-cultured osteosarcoma tumor spheroids were mixed with a 10 mg/ml fibrinogen solution and pre-crosslinked with 1 U/ml thrombin. The temperature of the nozzle was set at 20°C, and the printed structures were immersed in an AlgMA/GelMA bio-ink bath containing 0.5% photoinitiator. Printing was performed using a 16G needle at an extrusion speed of 15 μl/min. After printing, the structures were incubated in DMEM conditioned medium containing 1.8 mM calcium ions and subjected to UV crosslinking for 60 seconds.

Rheological and Mechanical Characterization

Rheology: The rheological properties of the prepolymers and hydrogels were assessed using a rheometer (Discovery HR20, TA, USA). A 20.0 mm parallel plate (Peltier plate stainless steel) was used for all measurements. To evaluate shear thinning, the record measure with the shear rate was increased from 0 to 100 s^{-1} at room temperature (25 °C). The frequency sweep assay was conducted on mixtures across a range of frequencies from 0.1 to 100 Hz, while maintaining a constant temperature of

25 ℃. During this process, both the storage modulus (G') and the loss modulus (G") were recorded.

Compression assay: Compression testing of the AlgMA/GelMA hydrogel was performed using a universal testing machine (AG-2000A, Japan). Prior to testing, the AlgMA/GelMA hydrogel was formed into a cylinder with a diameter of 5 mm. The compression modulus corresponds to the gradient of the initial linear segment observed on the stress-strain curves. The compression modulus of hydrogel is defined as stress/strain. In this study, the strain of the hydrogel is 10%-15%, representing a linear region that reflects the behavior of the hydrogel in the elastic phase. We performed linear fitting to calculate its compression modulus.

Atomic force microscopy (AFM)

Fibrin hydrogels based on the principle of human blood clotting are often characterized by weak mechanical properties. AFM can be used to characterize the elastic modulus of cellular materials and those with weak mechanical properties, owing to its ability to measure the mechanical properties of the sample surface at the nanoscale. The AFM probe touches the sample surface, applies small forces, and measures the response of the sample to these forces to determine its elastic modulus. The mechanical properties of osteosarcoma cells and fibrin hydrogels were assessed using Brooker AFM in the force curve scanning mode. This mode enables the measurement of the force–displacement relationship at various locations on the sample, allowing for the calculation of the elastic modulus of the sample. The resulting curve was fitted using the Hertz–Sneddon model to extrapolate the apparent Young's modulus. Data analysis was conducted using the Nanoscope Analysis software.

Scanning electron microscopy (SEM)and energy dispersive spectroscopy (EDS)

SEM was used to characterize the porosity of hydrogels with different concentration ratios. A tailored osteosarcoma model with an integrated gradient biomechanical signal of bioprinted constructs was observed using SEM (TESCAN, Czech Republic). Briefly, samples were fixed in glutaraldehyde at room temperature for 1 h and freeze-dried. The elemental distributions of the constructs were investigated by EDS (TESCAN, Czech Republic).

Cell counting kit-8 (CCK-8) assay

Effect of Ca^{2+} on the proliferation of 2D osteosarcoma cells: On day 0, MG-63 cells were plated in 96-well plates at a density of 2000 cells/well. Osteosarcoma cells were cultured in the conditioned medium with 0,0.9,1.8,2.7, and 3.6,4.5 mM calcium ions. On days 1, 3, and 5, cells were incubated with 100 μL of the conditioned medium containing 10% CCK-8 reagent (Beyotime, China) at 37 ℃ for 2 h. The absorbance of light at 450nm was detected utilizing an enzyme label (Synergy Neo2).

Effect of Ca^{2+} on the proliferation of osteosarcoma spheroid: Osteosarcoma cells were seeded in a 96-well cell culture plate with a U-bottom at a density of 2000 cells/well and incubated for 24 h. Subsequently, the medium was aspirated, and each well was replenished with the conditioned medium containing a calcium ion

concentration of either 0 or 1.8 mM. The absorbance at 450 nm was detected on days 1, 3, and 5 following the aforementioned protocol.

Fibrin hydrogel degradation test

Three groups of fibrin hydrogels were prepared using the molding method: fibrinogen and thrombin crosslinking, fibrinogen crosslinking with thrombin and transglutaminase, and fibrinogen crosslinking with thrombin and transglutaminase containing calcium ions. The initial mass of the fibrin hydrogel was recorded as W_0. Subsequently, 5 U/ml of lumbrokinase was added and incubated at 37 ℃ for 2 h, after which the weight was measured as W_1. The degradation rate of the fibrin hydrogel was calculated using the formula: $(W_0\text{-}W_1)\ /W_0 \times 100\%$.

Live/dead assay

The viability of the osteosarcoma model was evaluated using a live/dead cell staining kit (Yeasen, China) on the first and seventh days, as per the manufacturer's instructions. After removing the culture medium from the tumor model, the model underwent two washes with PBS. Subsequently, they were incubated in a solution containing 2 μM calcein acetoxymethyl (calcein-AM) and 4.5 μM propidium iodide (PI) for 30 minutes at 37°C, shielded from light exposure. Following removal of the dye solution under subdued lighting, the cells were rinsed twice with PBS. The samples were then examined using a laser-scanning confocal microscope (LSCM, Leica, Germany).

EDU proliferation experiment

The osteosarcoma model was first cultured in DMEM high-glucose medium for 24 hours. Afterward, the medium was removed, and the cells were washed with PBS. Subsequently, the cells were labeled using a 1:1000 dilution of EDU solution and incubated for 4 hours in a 37°C incubator. After labeling, the cells were fixed with 4% paraformaldehyde, and excess fixative was removed by washing with PBS. Next, the cells were permeabilized using 0.5% Triton X-100 solution and washed again with PBS. Following permeabilization, the cells were stained with Apollo staining solution and incubated for 30 minutes under light-avoidance conditions. After removing the excess staining solution by washing with PBS, the cell nuclei were stained with DAPI staining solution at a 1:1000 dilution and incubated for 10 minutes at room temperature under light-protected conditions. Finally, the cells were washed with PBS, observed, and photographed using a confocal microscope.

RNA extraction and RT-qPCR

OS and Ca^{2+}-OS samples were collected in a 15 ml centrifuge tube, centrifuged at 1000 rpm for 5 minutes, and then suspended in Trizol reagent. Ca^{2+}-S/OS and bioprinted Ca^{2+}-G/OS tumors were washed three times with PBS (1 minute each time), transferred to a 6-well plate containing an ophthalmic shear hydrogel, and thenTrizol reagent was added.

For genetic analysis, total RNA was isolated from the cells using Trizol reagent (Sangon Biotech, China). Reverse transcription was conducted to convert the extracted

mRNA into cDNA, utilizing the Prime Script RT kit (Yeasen, Shanghai) in conjunction with the SYBR Green RT-qPCR kit (Yeasen, Shanghai), followed by real-time PCR analysis using equipment from Thermo Fisher Scientific (USA). The procedures were performed in accordance with the manufacturer's guidelines, and the primer sequences for each gene can be found in Table S1 (Supporting Information).

Immunofluorescence

Four tumor models were established: OS, Ca^{2+}-OS, Ca^{2+}-S/OS, and Ca^{2+}-G/OS over a period of 4 days. Samples from each group were fixed with 4% paraformaldehyde for 20 minutes and subsequently washed three times with PBS. Following a 15-minute incubation with 0.5% Triton X-100 in PBS, the samples were then blocked in PBS containing 5% bovine serum albumin (BSA) for 1 hour. Primary anti- CD133 (1:400; Proteintech), anti-Vimentin (1:400; Proteintech), and anti-SOX2 (1:400; Proteintech) were applied overnight at 4 °C. Subsequently, secondary antibodies were incubated with the samples for 2 hours at room temperature. Finally, nuclei were stained with DAPI for 15 minutes. Observation was conducted using a LSCM.

Establishment and evaluation of in vivo tumor model

Before the experiment, the nude mice were weighed to calculate the appropriate amount of anesthetic. During the procedure, the mice's heads were tilted back slightly to move the lower abdominal organs upward. The injection site was sterilized using iodophor-soaked cotton balls. A 1% sodium pentobarbital solution, at a dose of 50 mg/kg, was injected into the lower abdomen of the mice, 0.5 cm on either side of the midline (level with the root of the thigh). The depth of anesthesia was confirmed by stimulating the toe response, after which the subsequent experiments were performed. Once disinfection was completed, the skin was incised and the four groups of osteosarcoma models that had been precultured for 4 days were implanted. After implantation, the tumors were closed using absorbable surgical sutures, and iodine povidone was applied to the wound sutures. The nude mice were then placed into cages and monitored for vital signs. Two weeks after tumor implantation, the nude mice were euthanized via cervical dislocation, and the tumor tissues were removed and transferred to 4% paraformaldehyde for subsequent histological evaluation.

This study was conducted in strict accordance with the guidelines of the Animal Care and Experimentation Committee of Shanghai Jiao Tong University. It was carefully evaluated and thoroughly reviewed by its expert group. After discussion and approval, the experimental protocol was formally authorized by the Animal Care and Experimentation Committee of Shanghai Jiao Tong University (Approval No. A2024001).

Histological Evaluations and immunofluorescence

The nude mice were euthanized 14 days after the tumor model was transplanted. The tumor tissues were removed and fixed with 4% paraformaldehyde. Sections (5 μm) were stained with H&E and immunofluorescence. Sections were fluorescently double-stained (CD133 and Ki67) to express tumor stem markers and finally scanned. Sections

were fluorescently double-stained (CD31, α-SMA) to examine the formation of tumor vessels and finally scanned. Sections were fluorescently stained (SOX2) to express tumor stem markers and scanned. For immunofluorescence, these slices were permeabilized with 0.3% Triton X-100 for 15 minutes. Subsequently, they were incubated with 5% BSA for 1 hour at room temperature to block nonspecific binding. Sections were incubated with anti-CD133 (1:400), anti-SOX2 (1:400), anti-Ki67 (1:400), anti-CD31 (1:400) and anti-α-SMA, (1:400) overnight at 4 °C. These sections were then incubated with secondary antibodies for 2 h at room temperature. Finally, DAPI was used to stain the cell nuclei for 15 minutes.

Drug permeability test and Chemotherapeutic drug efficacy

After PBS washing, 3D models were briefly exposed to Rhodamine B (10 μg/mL) for 3 h at 37 °C, followed by observation and imaging using a LSCM. Subsequently, tumor models were treated with varying concentrations (0, 0.1, 1, 10, 100, or 500 μM) of doxorubicin (Dox) and methotrexate (Mtx) for 48 h. Cell viability was assessed using the CCK8 assay.

RNA-seq analysis

The libraries were assembled in accordance with the guidelines provided by the manufacturer (BGI-Shenzhen, China). Bioinformatics analysis of RNA sequencing data was conducted using DR. TOM was provided by BGI. A heatmap was generated based on the expression levels of gene transcripts in different samples. Following the adjustment for significant pathway levels, KEGG enrichment and GSEA analysis was conducted on DEGs.

Statistical Analysis

The data are presented as mean ± standard deviation. Group differences were assessed using Tukey's post-hoc test and one-way analysis of variance (ANOVA). Statistical analyses were conducted using GraphPad Prism software. Statistical significance was defined as $*P < 0.05$, $**P < 0.01$, and $***P < 0.001$.

Results and Discussion

Design, Preparation, and Characterization of Bioink

The design and selection of bioinks are crucial steps in bioprinting, affecting the mechanical properties of tissues as well as cell behavior and function. Gelatin, derived from type I collagen, is a biocompatible biomaterial and a major component of the tumor ECM and bone microenvironment[28]. When reacted with methacrylic anhydride, gelatin is transformed into GelMA to produce photocrosslinkable hydrogels that are widely used to mimic the ECM in in vitro disease models [29]. Sodium alginate, a polysaccharide derived from natural seaweeds, is commonly used in bioinks because of its excellent biocompatibility. However, their poor mechanical properties limit their applications. As both the -OH and -COOH groups in its structural units can serve as reactive sites, sodium alginate can react with methacrylic anhydride to form AlgMA,

which has good biocompatibility and excellent mechanical properties. GelMA and AlgMA can undergo cross-linking reactions under ultraviolet light exposure, forming elastic, hydrophilic polymer networks with three-dimensional structures. Additionally, calcium ions form physical crosslinks with the carboxyl groups in AlgMA through electrostatic attraction, resulting in the formation of a physically crosslinked egg box structure [30]. The crosslinked MA groups contributed to the structural integrity of the hybrid hydrogel, whereas the physically crosslinked calcium ions formed a reversible network. Under stress, the UV light and the calcium ion-mediated dual-crosslinked interpenetrating network hydrogel dissipated energy, thereby enhancing its mechanical properties (Fig. 2a).

To optimize the interpenetrating network hydrogel and match the macroscopic collagenous bone tissue biomechanical signals, we investigated AlgMA concentrations of 1%, 2%, and 4% while keeping the GelMA concentration fixed at 10%. According to previous reports, 10% GelMA maintains cell viability, stimulates proliferation, and produces stable cultured gels, demonstrating higher proliferative capacity [31]. Rheological analysis of the three hydrogels showed that as the angular frequency varied from 1 to 100 rad s^{-1}, the interpenetrating polymer networks (IPNs) remained predominantly elastic, with no observed changes in G', indicating that the interpenetrating network hydrogel had stable elastic properties (Fig. 2b). The hybrid hydrogels of UV-crosslinked AlgMA and GelMA exhibited a storage modulus (G') greater than the loss modulus (G"), demonstrating typical characteristics of an elastic solid. This feature facilitates the construction of the complex three-dimensional microenvironment required for tumor growth.

Subsequently, the mechanical properties of the three interpenetrating network hydrogels were evaluated using a universal mechanical testing machine. Compressive moduli were calculated from the stress–strain curves, and the compressive moduli of the three interpenetrating network hydrogels were positively correlated with the AlgMA concentration. The compressive moduli of 1%, 2%, and 4% AlgMA–10% GelMA hydrogels were 42.16, 52.28, and 72.13 kPa, respectively (Fig. 2c). When the AlgMA concentration was 2%, the elastic modulus of the interpenetrating network hydrogel was 52.28 kPa, matching the macroscopic collagenous bone tissue biomechanical signal of 55 kPa [32]. The microstructures of the freeze-dried interpenetrating network hydrogels were analyzed using scanning electron microscopy (SEM). The hydrogels with three interpenetrating networks exhibited a loose porous microstructure, with the pore size becoming denser as the AlgMA concentration increased (Fig. 2d).

Fibrinogen molecules consist of α, β, and γ chains cross-linked by two sets of disulfide bonds. Each molecule comprises two external D domains linked to a central E domain through coiled coil segments. Thrombin cleaves fibrinopeptide A (FPA) from the fibrinogen Aα chain, triggering fibrin polymerization and the creation of a three-dimensional structure conducive to cell proliferation(Fig 2e)[33]. To construct a microenvironment mimicking the softness of osteosarcoma cells, we tested the Young's modulus of osteosarcoma cells using atomic force microscopy (AFM) with 620 Pa. Following the manufacturer's instructions, fibrin hydrogels were prepared using fibrinogen at concentrations of 10 mg/ml, 10 U/ml Th, and 3% w/v TG. The Young’s

modulus of the fibrin hydrogels, as characterized using AFM, was 657 Pa, with no statistically significant difference between the two ($P > 0.05$), indicating the successful construction of a microenvironment mimicking soft biomechanical signals (Fig. 2f). Furthermore, the rheological analysis revealed that the storage modulus of the fibrin hydrogels exceeded the loss modulus, exhibiting the characteristics of a solid-like material. This indicated its high elasticity and stability, providing essential three-dimensional structural support for osteosarcoma tumor spheroids (Fig. 2g). To further evaluate the printability of fibrin hydrogels, rheological tests were conducted over a shear rate range of 0.01 to 100 s^{-1}. The results showed that the fibrin hydrogels exhibited a shear-thinning behavior, indicating good rheological properties during the bioprinting process (Fig. 2h). Transglutaminase was added to the material system to further stabilize the fibrin hydrogels. Transglutaminase catalyzes the covalent crosslinking of proteins, leading to the formation of γ-glutamyl-ε-lysine side chain peptides and thus stabilizing the fibrin hydrogels[34]. Fibrin hydrogels were degraded using 10 U/ml lumbrokinase. The results showed that the degradation rate of the fibrin hydrogels containing only fibrinogen and thrombin was 91.36%, whereas those containing fibrinogen, thrombin, and transglutaminase had a degradation rate of 92.25%. Conversely, the degradation rate of fibrin hydrogels containing fibrinogen, thrombin, transglutaminase, and calcium ions was 83.86% (Fig. 2i). The degradation rates of fibrin hydrogels containing calcium ions were lower than those of the two previously mentioned fibrin hydrogel types ($P < 0.05$). In exploring the results of the fibrin hydrogel degradation experiments in Fig. 2i, we can take several perspectives. Firstly, concerning the degradation of fibrin hydrogels, we observed no statistically significant difference in degradation rates between fibrin hydrogels generated using fibrinogen and thrombin alone compared to those generated with the addition of transglutaminase (TGase) or with the further addition of calcium ions. This suggests that TGase alone has limited influence on the stability of fibrin hydrogels in the absence of calcium ions. Additionally, we found that when fibrinogen, thrombin, TGase, and calcium ions were combined, the resulting fibrin hydrogels exhibited a lower degradation rate. This indicates that calcium ions play a crucial role in enhancing the stability of fibrin hydrogels.

Calcium ions, as important divalent cations, play multiple crucial roles in the system used in this study. First, calcium ions underwent ion-exchange reactions with the carboxyl groups of the material, thereby promoting the formation of gel structures. This ion-exchange not only helps construct stable three-dimensional networks, but also imparts good structural integrity to the material. In particular, ion-exchange reactions with the carboxyl groups on AlgMA contribute to the formation of reversible networks, whereas physical crosslinking enhances the elasticity and durability of the hydrogels. Secondly, the addition of calcium ions activates transglutaminase, thereby facilitating the construction of stable fibrin hydrogels. Calcium ions serve as secondary messengers within cells and are crucial regulatory factors involved in multiple physiological and biochemical processes, including cell proliferation, apoptosis, and differentiation. During the previous literature research, we observed that calcium overload therapy has been widely emphasized in the field of oncology. In 2021, Yonglu Li and his team [35],

as well as Weier Bao et al[36], proposed calcium overload design strategies aimed at synergistic anti-tumor therapy. Given the role of calcium ions as a critical second messenger for cells, and the findings of Siew Shee Lim et al. [37] demonstrated that CTNTs scaffolds with added Ca^{2+} ions significantly enhanced their biocompatibility, we hypothesized that different concentrations of calcium ions may produce significant differences in the biological effects on osteosarcoma cells. Therefore, we explored various calcium ion concentrations in the present study to further reveal their potential effects. To determine the biological effects of calcium ions on osteosarcoma cells, the CCK-8 assay was employed to explore the proliferation of osteosarcoma cells treated with different concentrations of calcium ions at different time. The results of the CCK-8 assay showed that a stable concentration of 1.8 mM calcium ions significantly promoted OS cell proliferation (Fig. 2j). To evaluate the biological effects of calcium ions on osteosarcoma cells, osteosarcoma cells were cultured with 0 (control) and 1.8 mM (treat) calcium ions for 2 days, and RT-qPCR was used to detect the expression of genes related to the proliferation, migration, and stemness of osteosarcoma cells. Quantitative analysis showed that in the treatment group, the expression level of the proliferation-related gene MKI67 was significantly upregulated by 1.35-fold compared to that in the control group ($P<0.001$), whereas the expression levels of the anti-apoptotic gene BCL2 and the pro-apoptotic gene BAD were increased by 1.85-fold ($P<0.01$) and 1.3-fold ($P=0.0774$), respectively, compared to that in the control group. Furthermore, the relative expression levels of BCL2/BAD were normalized between the control group and treatment group, revealing that BCL2/BAD expression in the treatment group was 1.42-fold higher than that in the control group ($P<0.01$) (Fig. S1 a-d). Additionally, the expression levels of the migration-related genes Vimentin and CDH2 were 1.28-fold ($P<0.01$) and 1.39-fold ($P<0.001$) higher, respectively, in the treatment group than in the control group (Fig. S1 e-f). Moreover, the expression levels of the stemness-related genes, CD133 and SOX2, were 1.33-fold ($P=0.1428$) and 1.22-fold ($P<0.05$) higher, respectively, in the treatment group than in the control group (Fig. S1 g-h). Based on these results, we concluded that significant changes occurred in the biological characteristics of osteosarcoma cells in the calcium ion treatment group. In the treatment group, the expression levels of the proliferation-related gene MKI67 were significantly upregulated, and the expression levels of the anti-apoptotic gene BCL2 and pro-apoptotic gene BAD were also markedly increased. Furthermore, the expression of the migration-related genes Vimentin and CDH2 as well as the tumor stemness-related genes CD133 and SOX2 was significantly upregulated in the treatment group. These findings suggest that calcium ions can promote the proliferation and migration of osteosarcoma cells, inhibit tumor cell apoptosis, and regulate tumor stemness by affecting the expression of stemness genes. In addition, we investigated the effect of calcium ions on the proliferation of osteosarcoma tumor spheroids. The results of the CCK-8 assay demonstrated that calcium ions could stably promote the proliferation of osteosarcoma tumor spheroids over the long term (Fig. 2k).

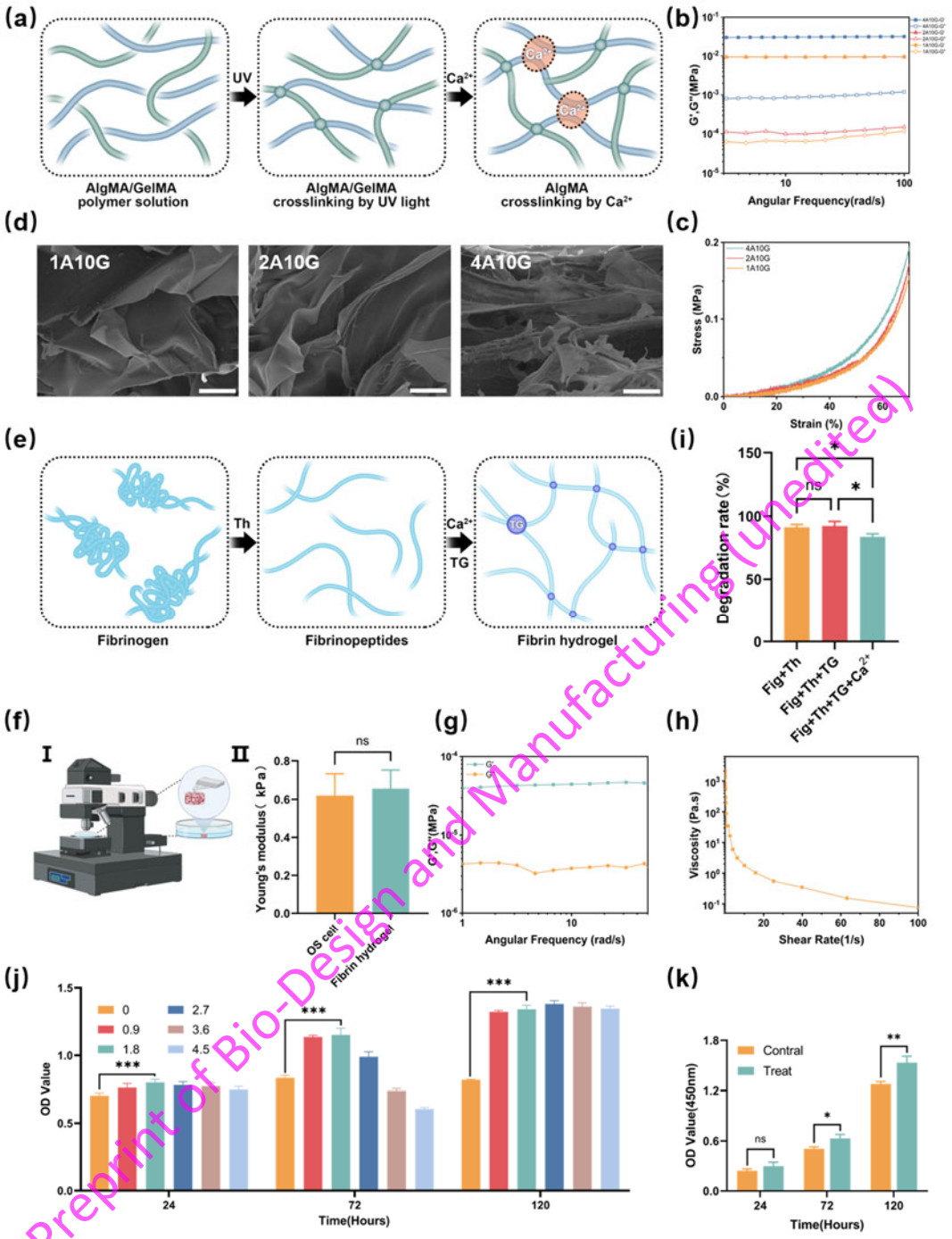

Fig. 2 Design, preparation, and characterization of bioinks. (**a**) Schematic illustration of the AlgMA/ GelMA hydrogel crosslinking mechanism. (**b**) Storage and loss moduli of AlgMA hydrogels at different concentrations. (**c**)Stress–strain curves of AlgMA hydrogels at different concentrations. (**d**) SEM morphology and porosity of AlgMA hydrogels at different concentrations (scale bar = 100 μm). (**e**) Schematic illustration of the fibrin hydrogel crosslinking mechanism. (**f**) Ⅰ Schematic representation of the Young's modulus characterization of fibrin hydrogels using AFM; Ⅱ Young's modulus of osteosarcoma cells and fibrin hydrogels . (**g**) Storage and loss moduli of the fibrin hydrogels. (**h**) Rheological properties of the fibrin hydrogels. (**i**) Degradation rates of three types of fibrin hydrogels. (**j**) Evaluation of osteosarcoma cell proliferation at

different calcium ion concentrations using the CCK-8 assay. (**k**) Evaluation of osteosarcoma tumor spheroid proliferation after calcium ion treatment using the CCK-8 assay.

Construction and Characterization of Integrated Gradient biomechanical Signal-Tailored Osteosarcoma Model

Pre-culture of Osteosarcoma Tumor Spheroids

Owing to the close resemblance of three-dimensional tumor spheroids to the gradient distribution of oxygen, nutrients, and metabolic byproducts in the in vivo environment as well as their characteristics of solid tumor density and high cell density, they have attracted increasing attention from researchers. To achieve this goal, we adopted a uniform and highly reproducible ultra-low attachment method for pre-culturing osteosarcoma tumor spheroids (Fig. 3a). Laser confocal microscopy confirmed the successful construction of the osteosarcoma three-dimensional tumor spheroids (Fig. S2a). According to previous reports by some researchers, when the diameter of tumor spheroids reaches approximately 400–600 μm, hypoxia due to oxygen and ATP deficiency occurs, resulting in the pathological physiological characteristics of solid tumors [38, 39]. Therefore, we preliminarily optimized the cell densities of osteosarcoma cells to 10,000 (SD-1), 20,000 (SD-2), and 30,000 (SD-3) for subsequent pre-culture experiments on osteosarcoma tumor spheroids (Fig. 3b). With increasing culture time, fluorescence microscopy observations at different time points showed that the area of the osteosarcoma tumor spheroids gradually decreased, the edges became smoother, and the spheroids became more compact. Subsequently, we used ImageJ to quantitatively analyze the circularity and area of osteosarcoma tumor spheroids at different time points and cell densities. The results showed that at a cell density of SD-2, the circularity of the osteosarcoma tumor spheroids cultured for 12, 24, and 36 h was 0.8, 0.87, and 0.87, respectively (1 indicates a perfect circle, 0 indicates a straight line). We found that circularity did not significantly increase with increasing culture time when osteosarcoma tumor spheroids were cultured for more than 24 h (Fig. S2b). Therefore, in subsequent experiments, we cultured the osteosarcoma tumor spheroids for 24 h. Furthermore, with prolonged culture time, the area of the osteosarcoma tumor spheroids decreased and became more compact (Fig. S2c). After pre-culturing the osteosarcoma tumor spheroids for 24 h at a cell density of SD-2, the diameter of the spheroids was approximately 550 μm, displaying the pathological physiological characteristics of solid tumors.

Characterization of the Integrated Gradient Biomechanical Signal-tailored Osteosarcoma Model

Fibrinogen loaded with osteosarcoma tumor spheroids was used as a bioink and embedded in a AlgMA/GelMA bioink bath to construct an integrated gradient biomechanical signal-tailored osteosarcoma model. After freeze-drying the constructed osteosarcoma model, SEM was used to characterize the microstructure of the integrated gradient biomechanical signal-tailored osteosarcoma model. SEM revealed a gradient of dense and loose gel pore microstructures (Fig. 3c). Moreover, SEM confirmed the

successful incorporation of osteosarcoma tumor spheroids into the gradient biomechanically signal-tailored hydrogel (Fig.3d). Furthermore, elemental analysis of common cellular elements using energy dispersive spectroscopy (EDS) demonstrated the successful construction of an integrated gradient biomechanical signal-tailored osteosarcoma model (Fig. 3e).

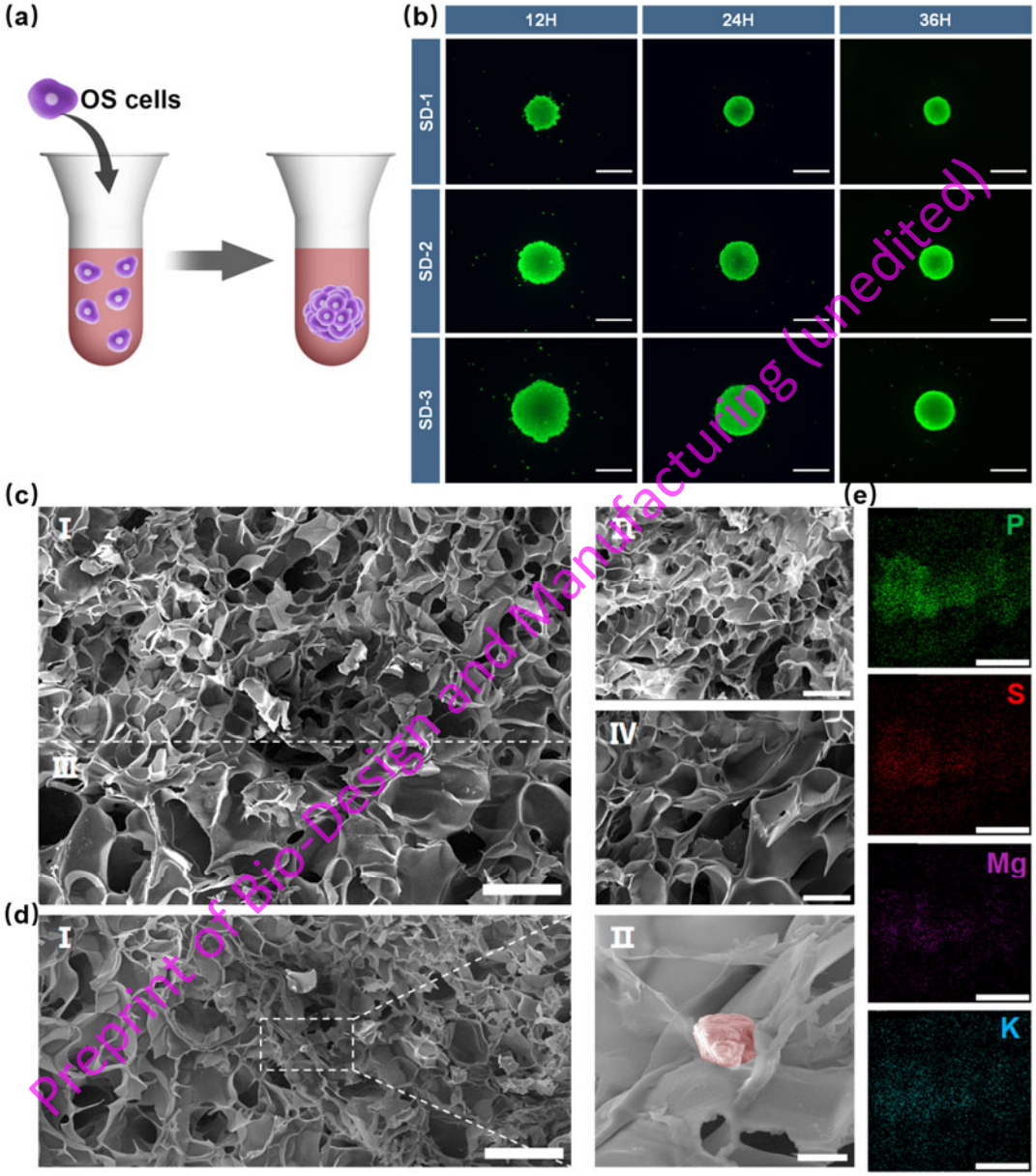

Fig. 3 Characterization of the Integrated Gradient Biomechanical Signal-tailored Osteosarcoma Model. (**a**) Schematic representation of osteosarcoma tumor spheroid culture. (**b**) Morphological characterization of osteosarcoma tumor spheroids under fluorescence microscopy (scale bar = 500 μm). (**c**) SEM characterization of the integrated gradient biomechanical signal-tailored osteosarcoma model (Ⅰ, Ⅲ scale bars = 200 μm; Ⅱ, Ⅳ scale bars = 100 μm). (**d**) Ⅰ Osteosarcoma tumor spheroid in the gradient model (scale bar = 200 μm). Ⅱ. Pseudo-staining of osteosarcoma tumor spheroid (scale bar = 20 μm). (**e**) EDS analysis of osteosarcoma tumor spheroid (scale

bar =15 μm).

In developing the model for this study, we focused on simulating the mechanics of osteosarcoma and successfully created a model capable of highly reproducing its mechanical properties. Compared to currently used models, our model represents a significant technological advancement in simulating the mechanical behavior of osteosarcoma. However, it is important to clarify that despite the success of our model in mechanical structure simulation, it does not fully capture the chemical structure of osteosarcoma. The chemical structure plays a crucial role in the complexity of osteosarcoma, influencing its unique properties such as reactivity, stability, and interactions with other substances. Therefore, while our model has made considerable progress in mechanistic simulation, it still has limitations in representing the chemical structure of osteosarcoma. We fully acknowledge this constraint and aim to address it in future studies. Enhancing our ability to simulate the chemical structure of osteosarcoma will enable us to gain a deeper understanding of its biological properties.

The osteosarcoma model tailored with integrated gradient biomechanical signals exhibits excellent biocompatibility.

Next, we characterized the biocompatibility of the osteosarcoma model using live/dead staining and EDU proliferation assays. Prior to the experiments, to further validate the biological effects of calcium ions in model construction and the effects of gradient biomechanical signaling in the customized osteosarcoma model, we divided the experiments into the following four groups: OS, Ca^{2+}-OS, Ca^{2+}-S/OS, and Ca^{2+}-G/OS. The OS group consisted of osteosarcoma spheroids without calcium ions. The Ca^{2+}-OS group included osteosarcoma spheroids with added calcium ions. The Ca^{2+}-S/OS group represented osteosarcoma spheroids embedded in a soft fibrin hydrogel containing calcium ions. The Ca^{2+}-G/OS group featured a 3D tumor model with a soft fibrin interior and a hard AlgMA/GelMA hydrogel exterior, constructed with calcium ions using 3D bioprinting.

First, we performed live/dead staining on the osteosarcoma model. We observed that on the first and seventh days of the experiment, the Ca^{2+}-OS, Ca^{2+}-S/OS, and Ca^{2+}-G/OS groups showed a limited number of dead cells, with significantly fewer dead cells than the OS group (Fig. 4a, Fig. S3a). Quantitative analysis using ImageJ revealed that on the first day, cell viability in the OS, Ca^{2+}-OS, Ca^{2+}-S/OS, and Ca^{2+}-G/OS groups was 79.93%, 91.19%, 89.97%, and 83.09%, respectively (Fig. S3b). The cell viability of the Ca^{2+}-OS group was significantly higher than that of the OS group ($P<0.01$), whereas that of the Ca^{2+}-G/OS group was only slightly higher than that of the OS group ($P>0.05$). On the seventh day, the cell viabilities in the OS, Ca^{2+}-OS, Ca^{2+}-S/OS, and Ca^{2+}-G/OS groups were 81.69%, 90.07%, 84.68%, and 85.04%, respectively (Figure S3C). The cell viability of the Ca^{2+}-OS group was significantly higher than that of the OS group($P<0.01$), and that of the Ca^{2+}-G/OS group was significantly higher than that of the OS group ($P<0.01$). These results indicated that Ca^{2+} can significantly reduce cell apoptosis in an osteosarcoma model, thereby enhancing the vitality of osteosarcoma cells and showing a trend of relative resistance to osteosarcoma cell apoptosis.

Next, we used EDU staining to assess cell proliferation in the osteosarcoma model. In EDU staining, cells undergoing DNA synthesis are labeled with bright green fluorescence, allowing the assessment of cell proliferation in the osteosarcoma model. The proliferation of osteosarcoma cells in the Ca^{2+}-OS, Ca^{2+}-S/OS, and Ca^{2+}-G/OS groups was higher than that in the OS group (Fig. 4b). In particular, in the Ca^{2+}-OS group, a significantly higher proportion of proliferating cells was observed than in the other groups, indicating a significant role of Ca^{2+} in promoting cell proliferation. Although the proliferation level of the Ca^{2+}-G/OS group was slightly lower than that of the Ca^{2+}-OS group, it was still significantly higher than that of the control group. In summary, our results demonstrated good biocompatibility of all osteosarcoma models in terms of live–dead staining and EDU staining. Particularly noteworthy is that the integrated gradient biomechanical signal-tailored osteosarcoma model exhibited high cell viability and proliferation capabilities, demonstrating excellent biocompatibility.

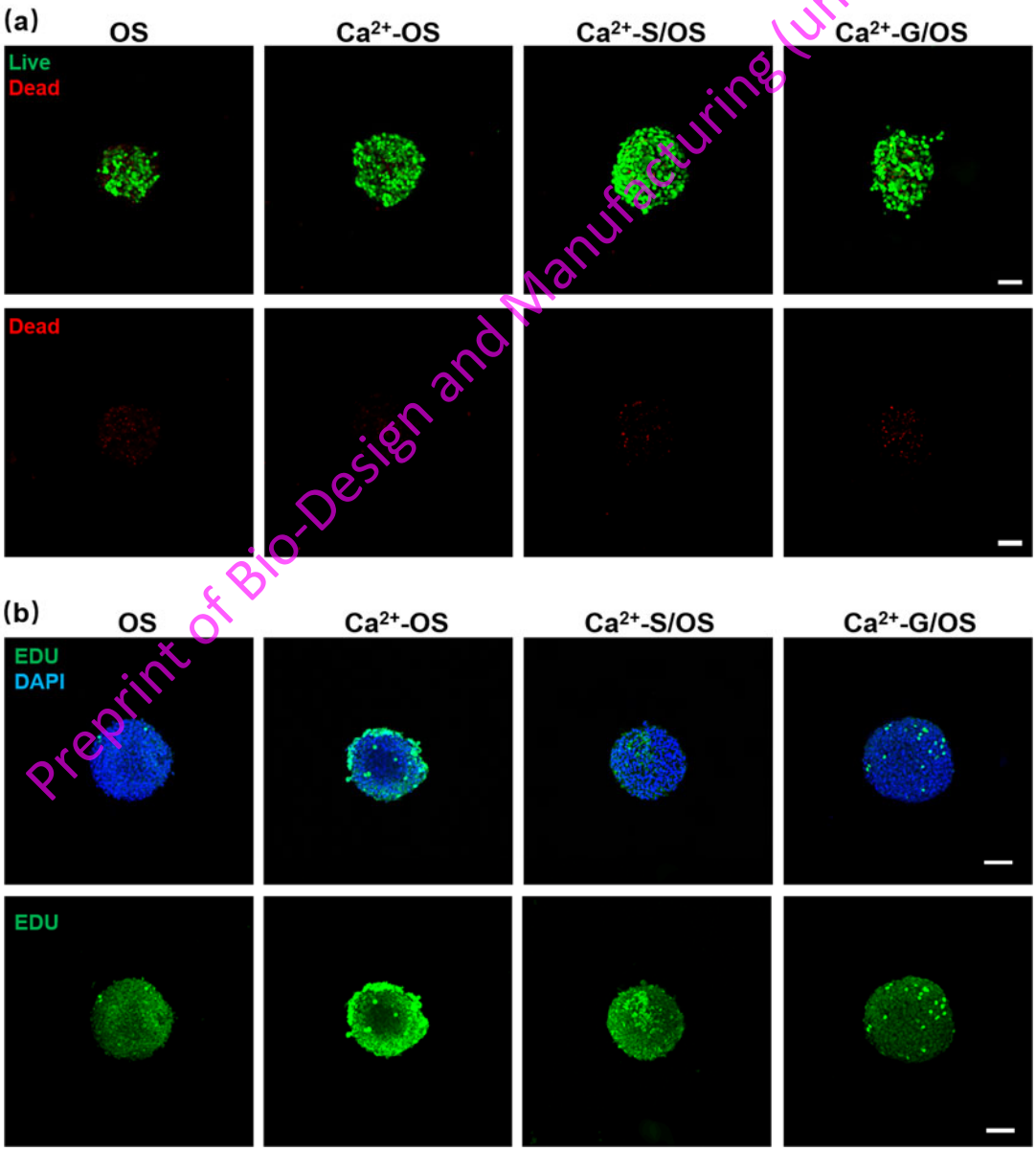

Fig. 4 Characterization of the biocompatibility of the osteosarcoma model. (**a**) Live–

dead staining of the osteosarcoma model on Day 1. The live cells are green, while the dead cells are red(scale bar = 100 μm). (**b**) Evaluation of proliferation in the osteosarcoma model using EDU staining (scale bar = 100 μm).

The Osteosarcoma Model Tailored with Integrated Gradient Biomechanical Signals Exhibits Stronger Phenotypes of Stemness, Migration, and Invasion.

Preservation of the natural biological characteristics of tumor cells in in vitro models is considered a crucial factor in tumor research. Tumors possess biological characteristics such as unlimited proliferation, uncontrolled growth, self-renewal, angiogenesis, resistance to apoptosis, invasion and metastasis, genetic variability, and immune evasion[40, 41]. The maintenance of tumor cell stemness is not only the basis for a deeper understanding of the pathogenesis of tumors but also a key factor in the development of new treatment strategies.

Next, we evaluated the expression of genes and proteins related to tumor stemness, migration, and invasion in an osteosarcoma model using RT-qPCR and immunofluorescence techniques. First, we assessed the expression of messenger RNA (mRNA) for tumor stemness-related marker genes (CD133 and SOX2) and tumor migration and invasion-related marker genes (Vimentin and CDH2) using RT-qPCR. RT-qPCR analysis showed that in the Ca^{2+}-G/OS group, the tumor stemness-related genes CD133 and SOX2 were 4.72-fold ($P<0.001$) and 2.1-fold ($P<0.001$) higher, respectively, than those in the OS group (Fig. 5a-b). The migration- and invasion-related genes, Snail2, Vimentin and CDH2, in the Ca^{2+}-G/OS group were1.6-fold ($P<0.001$),1.93-fold ($P<0.001$) and 2.6-fold ($P<0.001$) higher, respectively, than those in the OS group (Fig. S4b, Fig. 5c-d), whereas the difference in the expression of CDH1 was not statistically significant($P>0.05$) (Fig. S4a). These findings suggest that the integrated gradient biomechanical signal-tailored osteosarcoma model exhibits better stemness characteristics and stronger migration and invasion abilities. Additionally, we examined the mRNA expression levels of tumor proliferation-related genes (MKI67), anti-apoptotic genes (BCL2), and pro-apoptotic genes (BAD). RT-qPCR analysis showed that in the Ca^{2+}-G/OS group, the tumor proliferation-related gene MKI67 was 1.64-fold ($P<0.001$) higher, the anti-apoptotic gene BCL2 was 1.58-fold ($P<0.001$) higher, and the pro-apoptotic gene BAD was 0.55-fold ($P<0.001$) lower than in the OS group. Normalization of BCL2/BAD in the Ca^{2+}-G/OS group was 2.89-fold ($P<0.001$) higher than that in the OS group (Fig. S4c-f). These results suggested that the integrated gradient biomechanical signal-tailored osteosarcoma model exhibited enhanced proliferation promotion and apoptosis inhibition capabilities.

Subsequently, we characterized the expression of tumor stemness, migration, and invasion-related target proteins in all osteosarcoma models using immunofluorescence techniques. Immunofluorescence results showed that the levels of CD133, SOX2, and Vimentin in the Ca^{2+}-G/OS group were significantly higher than those in the other three groups (Fig. 5e-f, Fig. S5a-d), which was consistent with the gene expression of CD133, SOX2, and Vimentin. In summary, our results demonstrate that the integrated gradient biomechanical signal-tailored osteosarcoma model exhibits higher tumor stemness

characteristics, migration, and invasion capabilities while maintaining the biological characteristics of natural tumors.

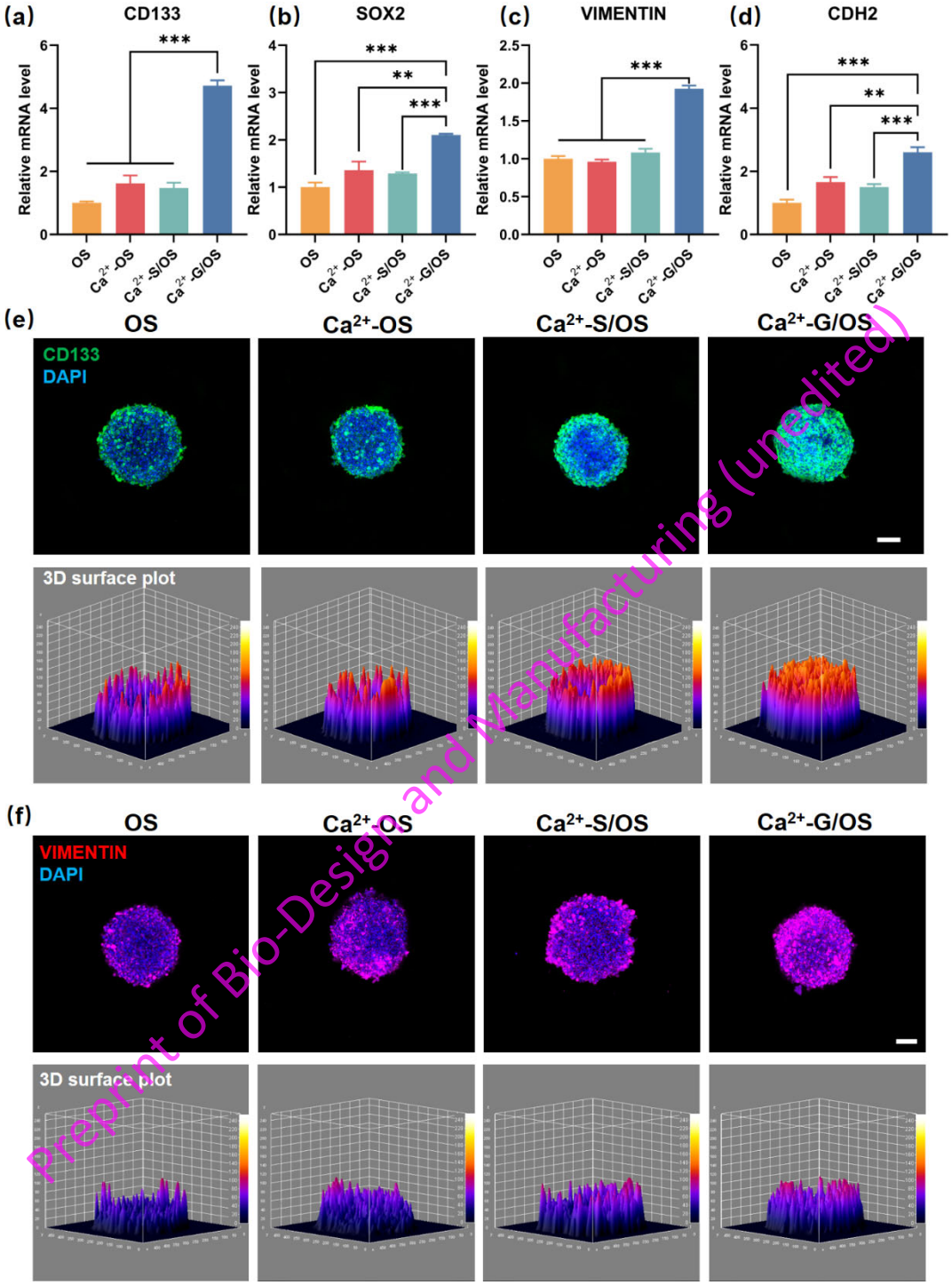

Fig. 5 Expression of tumor stemness and migration-related markers. (**a-b**) mRNA expression levels of tumor stemness markers CD133 and SOX2. (**c-d**) mRNA expression levels of migration markers Vimentin and CDH2. (**e-f**) Immunofluorescence images showing the expression of tumor stemness marker CD133 and migration marker Vimentin (scale bar = 100 μm).

Establishment of the Subcutaneous Osteosarcoma Model In Vivo

To assess the tumorigenic potential of the tumor models and preserve the innate biological characteristics of the implanted tumor cells, all osteosarcoma models were implanted subcutaneously into BALB/c nude mouse. Prior to implantation, we pre-cultured the four group tumor models for 4 days to allow the cells to fully adapt to the new growth environment. Fourteen days after implantation, we euthanized all animals, harvested the tumor tissues, and performed H&E and immunofluorescence staining (Fig. 6a). All the tumor models successfully formed tumors after implantation (Fig. 6b). The Ca^{2+}-OS group had the largest tumor volume, which may be due to the proliferative effect of calcium ions on osteosarcoma cells, and the Ca^{2+}-S/OS group had the smallest tumor volume, which may be due to its weak proliferative capacity, which is in line with the proliferative capacity of the ECM, which has been reported to be soft in the literature previously[42].

H&E staining revealed that osteosarcoma cells in all tumor models exhibited irregular morphology and deeply stained nuclei. Additionally, in the Ca^{2+}-S/OS and Ca^{2+}-G/OS groups, we observed a residual bioink that exhibited weak staining. Interestingly, in the Ca^{2+}-G/OS group, we observed the presence of nest-like structures formed by aggregated tumor cells (Fig. 6c). It is well known that in natural solid tumors, cancer cells have a tendency to aggregate into clusters or nests, forming structures commonly referred to as "cancer nests." These nest-like structures provide an organized tissue architecture that is conducive to close cellular arrangement and interactions, thereby promoting cell proliferation and infiltration and facilitating tumor growth and spread. The presence of nest-like structures is often associated with treatment resistance and is usually correlated with tumor malignancy and prognosis. Larger and more complex nest structures typically indicate higher invasive and metastatic potential and a poorer prognosis for tumors[43]. Therefore, in vitro tumor models reproducing cancer nest-like structures are of great significance for simulating the physiopathological characteristics of natural solid tumors, exploring the pathogenesis of cancer in depth, and evaluating the effectiveness of treatment.

Subsequently, we conducted immunofluorescence staining for tumor proliferation markers (Ki67), tumor stemness markers (CD133, SOX2), and vascular markers (CD31, α-SMA). In the Ca^{2+}-G/OS model, we observed a high expression of CD133 and Ki67 (Fig. 6d). Furthermore, another tumor stemness marker, SOX2, was expressed in all models but was significantly higher in the Ca^{2+}-G/OS osteosarcoma model than in the other groups (Fig. 6e). The expression of the vascular markers CD31 and α-SMA indicated that all four tumor models underwent vascularization, with larger vessel diameters observed in the OS and Ca^{2+}-G/OS groups compared to the Ca^{2+}-S/OS and Ca^{2+}-G/OS groups, possibly due to the hydrogel restricting vessel growth (Fig. 6f).

Based on these results, we conclude that the osteosarcoma model tailored with integrated gradient biomechanical signaling exhibits enhanced tumor stemness and proliferative activity and successfully recapitulates the cancer nest-like structures commonly found in tumor tissues. This discovery provides a solid experimental foundation for further exploration of tumor biology and the development of more effective treatment strategies.

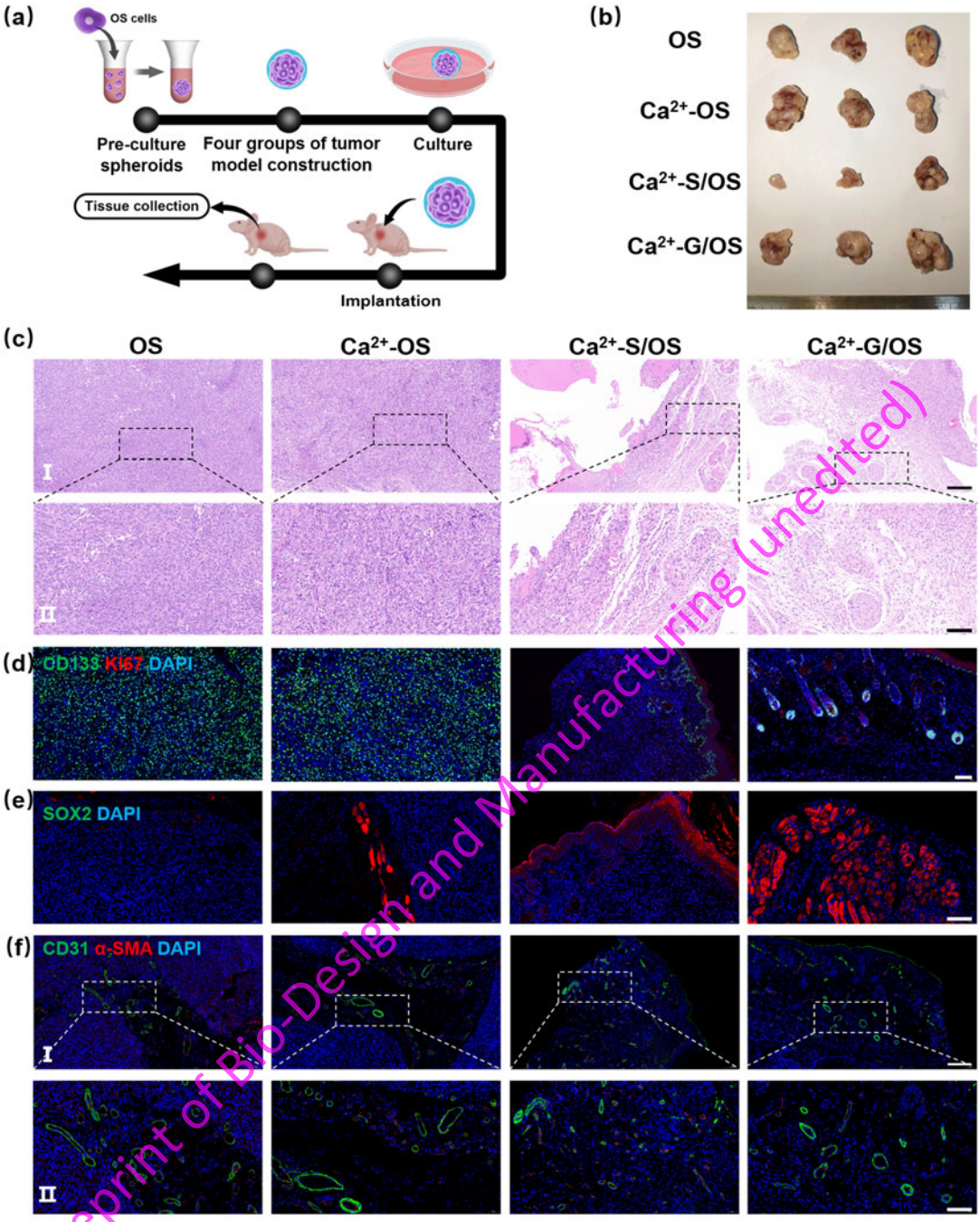

Fig. 6 In vivo subcutaneous assessment of osteosarcoma model establishment. (**a**) Schematic illustration depicting the entire process of animal testing. (**b**) Macroscopic view of the large tumor after collection. (**c**) H&E staining of the osteosarcoma models in each group (Ⅰ: scale bar = 100 μm, Ⅱ: scale bar = 50 μm). (**d-e**) Immunofluorescence images of tumor proliferation (KI67), stemness (CD133 and SOX2), scale bar = 50 μm. (**f**) Immunofluorescence images of vascular markers (CD31 and α-SMA) in the osteosarcoma models of each group (Ⅰ: scale bar = 100 μm, Ⅱ: scale bar = 50 μm).

In the previous sections, we detailed our research methods and results. To more fully assess the validity of our model and its results, we will now compare and discuss our findings with current widely used 3D models. First, our model has made significant technological advances in simulating the mechanics of osteosarcoma. Compared to traditional 2D tumor models and the 3D scaffold model for osteosarcoma tissue engineering developed by Eric R. Molina et al[44]., our model not only more accurately reproduces the high cell density of osteosarcoma-like tissues but also exhibits greater flexibility and precision in addressing the complex mechanical properties of osteosarcoma. This has enabled us to gain a deeper understanding of the behavior of osteosarcoma in both physiological and pathological states. Second, in comparing the ability of our model with existing 3D models in simulating the biological properties of osteosarcoma, we found that our model showed advantages in several aspects. For example, our model implanted in nude mice recapitulates the cancer nest-like structure of natural tumors and can simulate the interactions of osteosarcoma cells with the microenvironment more accurately. This precise simulation ability helps us to reveal the complex biological mechanisms of osteosarcoma and provides new ideas for developing more effective therapeutic approaches. However, although our model has demonstrated its unique value in some aspects, we are also conscious of its limitations compared to advanced 3D models developed by Fanben Meng and his team [45]. Their programmable release capsule, which accurately constructs tumor structures and enables precise spatio-temporal control of signaling molecular gradients, dynamically regulates cellular behaviors at the local level. In contrast, our model still has some limitations in key areas such as chemical structure simulation. Addressing these limitations will be the focus of our future research and improvement efforts.

In summary, we expect that, with continuous technological advances and deeper research, we will be able to develop even better models for the improved understanding and treatment of osteosarcoma.

The Osteosarcoma Model Tailored with Integrated Gradient Biomechanical Signals Demonstrates Greater Drug Resistance.

In vitro tumor models play a crucial role in drug development for basic research and clinical practice, demonstrating vast prospects and tremendous potential. These models not only faithfully mimic the complex biological characteristics of tumors but also provide efficient and cost-effective platforms for drug screening, thus offering crucial support for drug development and clinical translation research. Therefore, we conducted drug sensitivity tests on tumor models. Prior to this, we assessed the drug penetration of 3D tumor models using rhodamine B. with a molecular weight of 479.01, rhodamine B has a similar molecular weight to commonly used chemotherapeutic drugs, making it a suitable for chemotherapy drug simulations. Rhodamine B penetrated the entire 3D osteosarcoma model within 2 h, confirming good drug penetration of the 3D model (Fig. S6a). Subsequently, we performed drug sensitivity experiments using the tumor models. We selected the first-line chemotherapy drugs, doxorubicin and methotrexate, for drug sensitivity testing. Doxorubicin is an anthracycline anticancer chemotherapeutic drug that inhibits cancer cell growth and division by preventing DNA

replication and inducing apoptosis[46]. Methotrexate is an antimetabolite drug that inhibits dihydrofolate reductase in cells, reducing the levels of intracellular dihydrofolate and thereby affecting the synthesis of DNA and RNA, hindering cancer cell growth and division[47, 48]. The above-mentioned in vitro osteosarcoma models were co-incubated with different concentrations of methotrexate and doxorubicin (0, 0.1, 1, 10, 100, and 500 μM), and cell viability was evaluated after 48 h. The IC50 values of doxorubicin and methotrexate for Ca^{2+}-G/OS were 198 and 202.3 μM, respectively, while for the OS group, these values were 22.09 and 57.16 μM, respectively. The Ca^{2+}-G/OS group exhibited higher drug resistance (Fig. 7a-b). This phenomenon may be related to the enhanced stemness of tumor Ca^{2+}-G/OS cells, which increases their drug resistance.

To further validate the feasibility of the integrated gradient biomechanical signal-tailored tumor model and explore its potential mechanisms, we conducted transcriptome sequencing analysis. This work aims to comprehensively analyze the gene expression profile in the tumor model and conduct a comprehensive analysis and investigation of the potential signaling pathways and regulatory networks involved. Through this in-depth transcriptomic study, we hope to reveal the molecular mechanisms underlying the formation of a tumor model, providing an important theoretical and experimental basis for further biological research and clinical treatment. Transcriptome analysis was performed on the Ca^{2+}-G/OS and OS groups of osteosarcoma models using RNA sequencing technology to study molecular changes in depth. Using RNA deep sequencing, we compared the OS and Ca^{2+}-G/OS groups of the models, revealing 380 upregulated and 339 downregulated genes, respectively (Fig.S6b). This indicates significant gene expression changes between the two, laying the foundation for further exploration of the molecular mechanisms in osteosarcoma models.

To deeply explore the patterns of differentially expressed genes (DEGs), we performed a systematic cluster analysis (Fig.7c). This analysis aimed to reveal patterns of gene expression and cluster affiliation, thereby enhancing our understanding of the regulatory network of DEGs. To further elucidate the functions and potential pathways of these DEGs, we performed KEGG pathway enrichment analysis. By examining the top 15 significantly enriched pathways, we gained insights into the functions of DEGs. The results of the enrichment analysis suggest that these DEGs may be involved in key biological processes such as DNA replication, the cell cycle, and the hedgehog signaling pathway (Fig.7d). This suggests that the integrated gradient mechanics microenvironmental osteosarcoma model significantly impacts these signaling pathways. In particular, the regulatory mechanisms of DNA replication and the cell cycle are central to various tumor-associated signaling pathways. Additionally, the enrichment of the HH signaling pathway suggests that this pathway may play a key role in osteosarcoma genesis, development, and signature expression.

In the present study, the Ca^{2+}-G/OS group showed enhanced resistance to chemotherapeutic agents compared with the OS group. In light of recent findings on the supportive role of the biomechanical environment for cancer stem cells (CSCs), niche stiffness maintains cancer stemness through the phase separation of TAZ and

NANOG. Therefore, we hypothesized that Ca^{2+}-G/OS osteosarcomas may enrich tumor stem cells, thereby enhancing their resistance to chemotherapeutic agents[49]. To more fully explore the impact of mechanical signaling on cellular phenotype and function, we conducted an in-depth analysis of the transcriptome data and introduced gene set enrichment analysis (GSEA). As shown in Figure S6c, while the MAPK signaling pathway was more likely to be identified as a potential therapeutic target, this does not mean that mechanical signaling does not play a role. When GSEA assesses gene set enrichment, the trends of the genes are taken into account. As some genes are upregulated while others are downregulated, this may result in an attenuated enrichment signal for that gene set in the GSEA analysis. Therefore, GSEA may have failed to show a significant enrichment effect. However, this analysis still provides valuable insights and guides the direction of future studies.

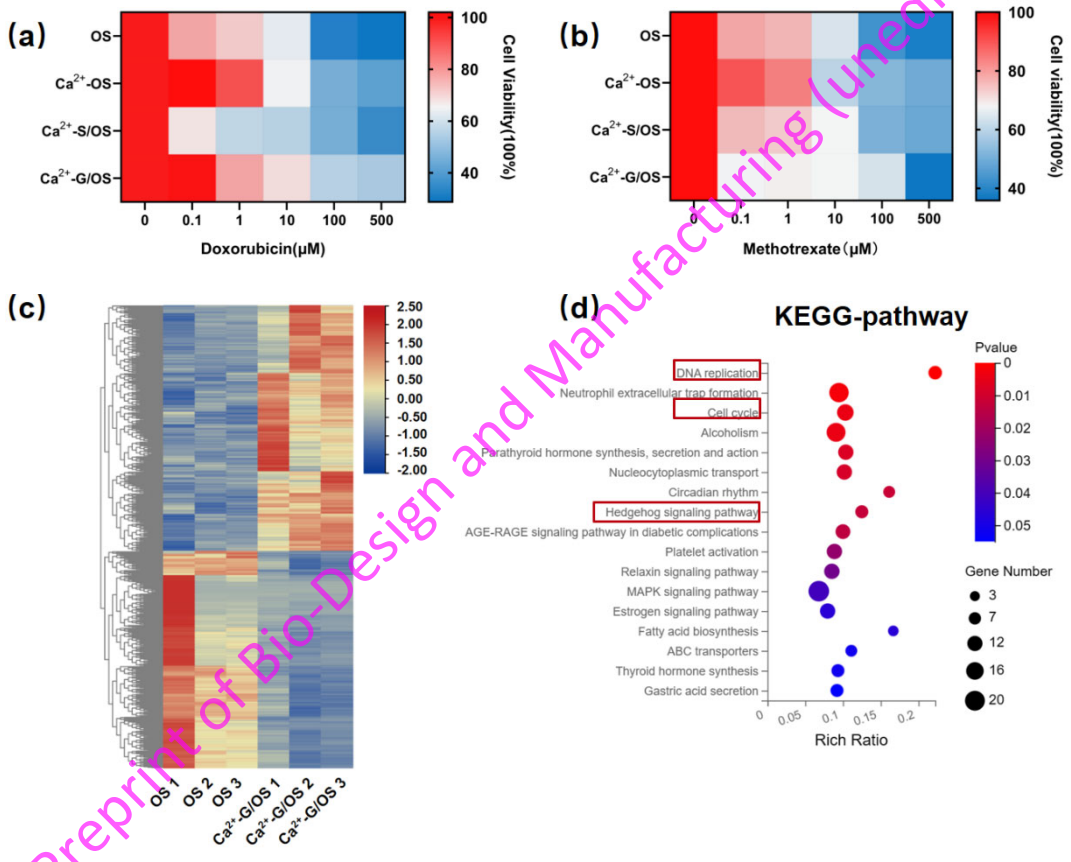

Fig. 7 Drug sensitivity and transcriptome analysis of the in vitro osteosarcoma model. (**a-b**) The sensitivity of doxorubicin and methotrexate to drugs. (**c**) Heatmap of DEGs clustering. (**d**) Enrichment analysis of DEGs using KEGG pathways. The pathways of interest are highlighted in red boxes.

Conclusions

To the best of our knowledge, this is the first study to successfully construct a gradient biomechanical signal-tailored osteosarcoma model that reproduces the pathophysiological features of osteosarcoma. Using advanced bioprinting equipment, we carefully designed and optimized a bioink to construct a highly integrated

biomechanical signal-tailored osteosarcoma model. Notably, the bioprinted osteosarcoma model not only accurately mimicked the gradient biomechanical signal properties of osteosarcoma but also exhibited more significant tumor stemness, proliferation, and migration. Importantly, the model successfully reproduced the pathophysiological characteristics of cancer nest-like structures in a natural tumor model, providing strong support for our in-depth understanding of the pathogenesis of osteosarcoma. In addition, transcriptome analysis revealed the potential regulatory pathways of gradient biomechanical signaling in the osteosarcoma model, providing valuable clues for subsequent drug screening, therapeutic studies, and exploration of drug resistance and metastasis mechanisms. In summary, this study provides a highly valuable research platform for an in-depth understanding of the pathogenesis of osteosarcoma, drug screening, therapeutic studies, and the exploration of drug resistance and metastasis mechanisms.

Supporting Information

Support information is available online.

Acknowledgment

X.M., Y.R., and H. W. contributed equally to this work. The authors appreciate financial support from the National Key R&D Program of China (2022YFA1104600), 2022 Lingang laboratory "Seeking Outstanding Youth Program" open project (LGQS-202206-04), Shanghai Ninth People's Hospital-Shanghai JiaoTong University School of Medicine-Shanghai University of Science and Technology Cross-funded Collaborative Program" (JYJC202233), National Natural Science Foundation of China (82372377), Biomaterials and Regenerative Medicine Institute Cooperative Research Project by Shanghai JiaoTong University School of Medicine (grant number 2022LHBO8), Shanghai Key Laboratory of Orthopedic Implant, Department of Orthopedics(No.KFKT202206)， the Key R&D Program of Jiangsu Province Social Development Project (BE2022708), Project of Shanghai Science and Technology Commission (22015820100). We thank S.S. and J. Z. for their help with this study. We would like to express our gratitude to the Biorender for its valuable assistance in creating figures for this manuscript.

Conflict of Interest

The authors declare no conflict of interest.

Data Availability Statement

The data that support the findings of this study are available from the corresponding author upon reasonable request.

References

[1] J. S. Biermann, et al.(2017) NCCN Guidelines Insights: Bone Cancer, Version 2.2017.Journal of the National Comprehensive Cancer Network J Natl Compr Canc Netw.2(15):155-167.https://doi.org/10.6004/jnccn.2017.0017

[2] B. J. Miller, et al.(2013) Risk factors for metastatic disease at presentation with osteosarcoma: an analysis of the SEER database.J Bone Joint Surg Am.13(95):e89.https://doi.org/10.2106/JBJS.L.01189

[3] A. Birgersdotter, et al. (2005) Gene expression perturbation in vitro--a growing case for three-dimensional (3D) culture systems.Semin Cancer Biol.5(15):405-12.https://doi.org/10.1016/j.semcancer.2005.06.009

[4] A. Astashkina, et al. (2012) A critical evaluation of in vitro cell culture models for high-throughput drug screening and toxicity.Pharmacol Ther.1(134):82-106.https://doi.org/10.1016/j.pharmthera.2012.01.001

[5] R. S. Stowers, et al. (2019) Matrix stiffness induces a tumorigenic phenotype in mammary epithelium through changes in chromatin accessibility.Nat Biomed Eng.12(3):1009-1019.https://doi.org/10.1038/s41551-019-0420-5

[6] K. M. Wisdom, et al. (2018) Matrix mechanical plasticity regulates cancer cell migration through confining microenvironments.Nat Commun.1(9):4144.https://doi.org/10.1038/s41467-018-06641-z

[7] S. Safaei, et al. (2023) Tumor matrix stiffness provides fertile soil for cancer stem cells.Cancer Cell International.1(23):143.https://doi.org/10.1186/s12935-023-02992-w
[8] Y. Sun, et al. (2021) The distribution of liver cancer stem cells correlates with the mechanical heterogeneity of liver cancer tissue.Histochemistry and Cell Biology.1(156):47-58.https://doi.org/10.1007/s00418-021-01979-w
[9] W. Xu, et al. (2012) Cell stiffness is a biomarker of the metastatic potential of ovarian cancer cells.
[10] M. Plodinec, et al. (2012) The nanomechanical signature of breast cancer.11(7):757-765.https://doi.org/
[11] J. M. M. Cates,J. G. Schoenecker (2016) Proximal location in extremity long bones is a poor prognostic factor for osteosarcoma: A retrospective cohort study of 153 patients.Acta Oncologica.8(55):1036-1039.https://doi.org/10.3109/0284186X.2016.1156740
[12] J. M. Northcott, et al. (2018) Feeling Stress: The Mechanics of Cancer Progression and Aggression.Front Cell Dev Biol.6):17.https://doi.org/10.3389/fcell.2018.00017
[13] T. Chow, et al. (2021) Creating In Vitro Three-Dimensional Tumor Models: A Guide for the Biofabrication of a Primary Osteosarcoma Model.Tissue Eng Part B Rev.5(27):514-529.https://doi.org/10.1089/ten.TEB.2020.0254
[14] N. Leitner, et al. (2022) Lipid droplets and perilipins in canine osteosarcoma. Investigations on tumor tissue, 2D and 3D cell culture models.Veterinary research communications.4(46):1175-1193.https://doi.org/10.1007/s11259-022-09975-8
[15] J. Ren, et al. Augmented drug resistance of osteosarcoma cells within decalcified bone matrix scaffold: The role of glutamine metabolism.n/a(n/a):https://doi.org/10.1002/ijc.34841
[16] J. He, et al. (2022) Honeycomb-Like Hydrogel Microspheres for 3D Bulk Construction of Tumor Models.Research (Wash D C).2022):9809763.https://doi.org/10.34133/2022/9809763
[17] P. S. Gungor-Ozkerim, et al. (2018) Bioinks for 3D bioprinting: an overview.Biomaterials science.5(6):915-946.https://doi.org/10.1039/C7BM00765E
[18] A. Mousavi, et al. (2024) Development of photocrosslinkable bioinks with improved electromechanical properties for 3D bioprinting of cardiac BioRings.Applied Materials Today.36):102035.https://doi.org/https://doi.org/10.1016/j.apmt.2023.102035
[19] A. Parak, et al. (2019) Functionalizing bioinks for 3D bioprinting applications.Drug Discovery Today.1(24):198-205.https://doi.org/https://doi.org/10.1016/j.drudis.2018.09.012
[20] B. Cao, et al.(2023) 3D-printed vascularized biofunctional scaffold for bone regeneration.3(9):10.18063/ijb.702
[21] I. Pereira, et al. (2023) Hyaluronic acid-based bioink improves the differentiation and network formation of neural progenitor cells.11):10.3389/fbioe.2023.1110547
[22] D. Wang, et al. (2022) Microfluidic bioprinting of tough hydrogel-based

vascular conduits for functional blood vessels.Science advances.43(8):eabq6900.https://doi.org/10.1126/sciadv.abq6900
[23] H. Chen, et al. (2023) Injectable and biofunctionalized fibrin hydrogels co-embedded with stem cells induce hair follicle genesis.Regen Biomater.10):rbac086.https://doi.org/10.1093/rb/rbac086
[24] S. V. Murphy,A. Atala (2014) 3D bioprinting of tissues and organs.Nature Biotechnology.8(32):773-785.https://doi.org/10.1038/nbt.2958
[25] P. Datta, et al. (2020) 3D bioprinting for reconstituting the cancer microenvironment.npj Precision Oncology.1(4):18.https://doi.org/10.1038/s41698-020-0121-2
[26] A. C. Daly, et al. (2021) Bioprinting for the Biologist.Cell.1(184):18-32.https://doi.org/https://doi.org/10.1016/j.cell.2020.12.002
[27] X. Cui, et al. (2017) Advances in multicellular spheroids formation.J R Soc Interface.127(14):10.1098/rsif.2016.0877
[28] E. Shams, et al. (2022) A review on alginate-based bioinks, combination with other natural biomaterials and characteristics.2(37):355-372.https://doi.org/10.1177/08853282221085690
[29] D. Loessner, et al. (2016) Functionalization, preparation and use of cell-laden gelatin methacryloyl–based hydrogels as modular tissue culture platforms.Nature Protocols.4(11):727-746.https://doi.org/10.1038/nprot.2016.037
[30] L. Li, et al. (2007) Reexamining the Egg-Box Model in Calcium−Alginate Gels with X-ray Diffraction.Biomacromolecules.2(8):464-468.https://doi.org/10.1021/bm060550a
[31] A. D. Arya, et al. (2016) Gelatin Methacrylate Hydrogels as Biomimetic Three-Dimensional Matrixes for Modeling Breast Cancer Invasion and Chemoresponse in Vitro.ACS Applied Materials & Interfaces.34(8):22005-22017.https://doi.org/10.1021/acsami.6b06309
[32] E. Mylona, et al. (2008) SUBSTRATE RIGIDITY DICTATES PHENOTYPE, SURVIVAL, AND MECHANICS OF PRIMARY HUMAN OSTEOSARCOMA CELLS.
[33] M. W. Mosesson (2005) Fibrinogen and fibrin structure and functions.J Thromb Haemost.8(3):1894-904.https://doi.org/10.1111/j.1538-7836.2005.01365.x
[34] L. Lorand,S. M. Conrad (1984) Transglutaminases.Molecular and Cellular Biochemistry.1(58):9-35.https://doi.org/10.1007/BF00240602
[35] Y. Li, et al. (2021) CaCO3 nanoparticles incorporated with KAE to enable amplified calcium overload cancer therapy.Biomaterials.277):121080.https://doi.org/https://doi.org/10.1016/j.biomaterials.2021.121080
[36] W. Bao, et al. (2021) MOFs-based nanoagent enables dual mitochondrial damage in synergistic antitumor therapy via oxidative stress and calcium overload.Nature Communications.1(12):6399.https://doi.org/10.1038/s41467-021-26655-4
[37] S. S. Lim, et al. (2017) In vitro evaluation of osteoblast adhesion, proliferation and differentiation on chitosan-TiO2 nanotubes scaffolds with Ca2+

ions.Materials Science and Engineering: C.76):144-152.https://doi.org/https://doi.org/10.1016/j.msec.2017.03.075
[38] A. Bertuzzi, et al. (2010) Necrotic core in EMT6/Ro tumour spheroids: Is it caused by an ATP deficit?J Theor Biol.1(262):142-50.https://doi.org/10.1016/j.jtbi.2009.09.024
[39] S. Nath,G. R. Devi (2016) Three-dimensional culture systems in cancer research: Focus on tumor spheroid model.Pharmacol Ther.163):94-108.https://doi.org/10.1016/j.pharmthera.2016.03.013
[40] Y. Zhao, et al. (2018) Targeting cancer stem cells and their niche: perspectives for future therapeutic targets and strategies.Seminars in Cancer Biology.53):139-155.https://doi.org/https://doi.org/10.1016/j.semcancer.2018.08.002
[41] T. Reya, et al. (2001) Stem cells, cancer, and cancer stem cells.6859(414):105-111.https://doi.org/
[42] S. Li, et al. (2020) Soft Substrate Promotes Osteosarcoma Cell Self-Renewal, Differentiation, and Drug Resistance Through miR-29b and Its Target Protein Spin 1.ACS Biomater Sci Eng.10(6):5588-5598.https://doi.org/10.1021/acsbiomaterials.0c00816
[43] F. Arienzo, et al. (2024) Metastatic upper tract urothelial carcinoma with nest-like features presenting as malignant pleural effusion.Diagnostic cytopathology.10.1002/dc.25293
[44] E. R. Molina, et al. (2019) Mechanically tunable coaxial electrospun models of YAP/TAZ mechanoresponse and IGF-1R activation in osteosarcoma.Acta Biomater.100):38-51.https://doi.org/10.1016/j.actbio.2019.09.029
[45] F. Meng, et al. (2019) 3D Bioprinted In Vitro Metastatic Models via Reconstruction of Tumor Microenvironments.10(31):1806899.https://doi.org/https://doi.org/10.1002/adma.201806899
[46] J. L. Nitiss (2009) Targeting DNA topoisomerase II in cancer chemotherapy.Nature reviews. Cancer.5(9):338-50.https://doi.org/10.1038/nrc2607
[47] B. Gallego, et al. (2022) Addressing Doxorubicin Resistance in Bone Sarcomas Using Novel Drug-Resistant Models.Int J Mol Sci.12(23):10.3390/ijms23126425
[48] C. Meazza,S. D. Asaftei (2021) State-of-the-art, approved therapeutics for the pharmacological management of osteosarcoma.Expert opinion on pharmacotherapy.15(22):1995-2006.https://doi.org/10.1080/14656566.2021.1936499
[49] X. Liu, et al. (2023) Niche stiffness sustains cancer stemness via TAZ and NANOG phase separation.Nature Communications.1(14):238.https://doi.org/10.1038/s41467-023-35856-y